Tunable coupling of terahertz Dirac plasmons and phonons in transition metal dichalcogenide-based van der Waals heterostructures

Tunable coupling of terahertz Dirac plasmons and phonons in transition-metal dichalcogenide-based van der Waals heterostructures

I. R. Lavor,[1,2,3,*] Andrey Chaves,[2,3] F. M. Peeters,[3] and B. Van Duppen[3,†]

[1] *Instituto Federal de Educação, Ciência e Tecnologia do Maranhão, KM-04, Enseada, 65200-000, Pinheiro, Maranhão, Brazil*
[2] *Departamento de Física, Universidade Federal do Ceará, Caixa Postal 6030, Campus do Pici, 60455-900 Fortaleza, Ceará, Brazil*
[3] *Department of Physics, University of Antwerp, Groenenborgerlaan 171, B-2020 Antwerp, Belgium*

(Dated: November 8, 2021)

Dirac plasmons in graphene hybridize with phonons of transition metal dichalcogenides (TMDs) when the materials are combined in so-called van der Waals heterostructures (vdWh), thus forming surface plasmon-phonon polaritons (SPPPs). The extend to which these modes are coupled depends on the TMD composition and structure, but also on the plasmons' properties. By performing realistic simulations that account for the contribution of each layer of the vdWh separately, we calculate how the strength of plasmon-phonon coupling depends on the number and composition of TMD layers, on the graphene Fermi energy and the specific phonon mode. From this, we present a semiclassical theory that is capable of capturing all relevant characteristics of the SPPPs. We find that it is possible to realize both strong and ultra-strong coupling regimes by tuning graphene's Fermi energy and changing TMD layer number.

I. INTRODUCTION

In the past few years, after the advent of graphene [1], a two-dimensional (2D) monolayer of carbon atoms arranged in a honeycomb lattice, the interest of the scientific community in isolating and studying new 2D materials has been significantly increasing due to the unique features of these materials [2–4]. For example, 2D transition metal dichalcogenides (TMDs) [5, 6], which present a MX_2 form, with a metal (M) layer surrounded by two layers of a chalcogen (X), such as MoS_2, $MoSe_2$, WS_2 and WSe_2, have attracted considerable attention due to their remarkable opto-electronic properties [3, 4, 7–15] that arises, for example, due to their electronic band gaps [16, 17], the specific type of the electronic structure, and the intrinsic mobility of the electrons [18]. These 2D materials can be combined in so-called van der Waals heterostructures (vdWh) [3, 19, 20] by stacking different layers on top of each other [3, 5, 7, 11, 12, 15, 21], or even next to each other forming so-called lateral heterostructures [5, 21–26], resulting in the creation of many different multi-layered artificial materials, each with specific behaviour [20, 27]. Recently, significant advances have been made to obtain and manufacture such heterostructures [3, 5–7, 12, 20–27].

Graphene plasmons, collective excitations of the 2D electron liquid in graphene [28, 29], also known as Dirac plasmons [30], are heavily studied due to their low loss [31, 32], a frequency that is tunable by the Fermi energy [13, 14, 33, 34] and their possible applications in photonics [30, 35, 36]. Besides, graphene can support plasmons at mid-infrared (mid-IR) [8, 37, 38] to terahertz (THz) frequencies [8, 13, 39, 40] and show strong electromagnetic field confinement [30, 41]. On the other hand, in TMDs (such as MoS_2 or WS_2, for example), active modes reside in the mid-IR range [42] and, due to their large electronic band gap [17, 43], these materials behave as dielectrics at low frequencies, thus not supporting plasmons if not extrinsically doped [44].

As illustrated in Fig. 1(a), when a monolayer graphene (MLG) is combined with layers of TMDs, forming graphene-based vdWhs, a hybrid excitation arises that is known as surface plasmon-phonon polaritons (SPPPs). These quasiparticles are formed when phonons in the TMDs are coupled to the electron oscillations in graphene [41]. One can excite and measure them using scatter-type scanning near-field optical microscopy (s-SNOM) [40, 45, 46]. This allows one to measure the SPPPs wavelength, with a resolution of up to 20 nm [14, 33, 45–50], using interference fringes formed by the scattering of SPPPs modes at the edge of the heterostructure or at lateral defects in the system. Although monolayer 2H-TMDs, where 2H refers to the hexagonal symmetry [7], have four non-degenerate optical phonon modes in the infrared (IR) spectrum, only two of them, namely, the in-plane E' , which is IR and Raman (R) active, and out-of-plane A_2'' (IR), illustrated in Fig. 1(b), can couple to Dirac plasmons [42, 51, 52]. In the case of an even number of stacked TMD layers, the E' and A_2'' modes of 1L-MX_2 and other systems with odd number of layers, split into E_u (IR) and E_g^1 (R), and A_{2u} (IR) and A_{1g}^1 (R) modes, respectively. [42]. For completeness, Appendix A provides a description of N-layer 2H-TMDs phonon modes at Γ-point, while an illustration of all vibrational phonon modes in this type of heterostructure can be found in Refs [42] and [52].

In analogy to two coupled harmonic oscillators [53], Fig. 1(c), when graphene plasmons and TMDs phonons are coupled, the eigenfrequencies of the system are modified, presenting a characteristic anti-crossing [54, 55], as

* icaro@fisica.ufc.br
† ben.vanduppen@uantwerpen.be

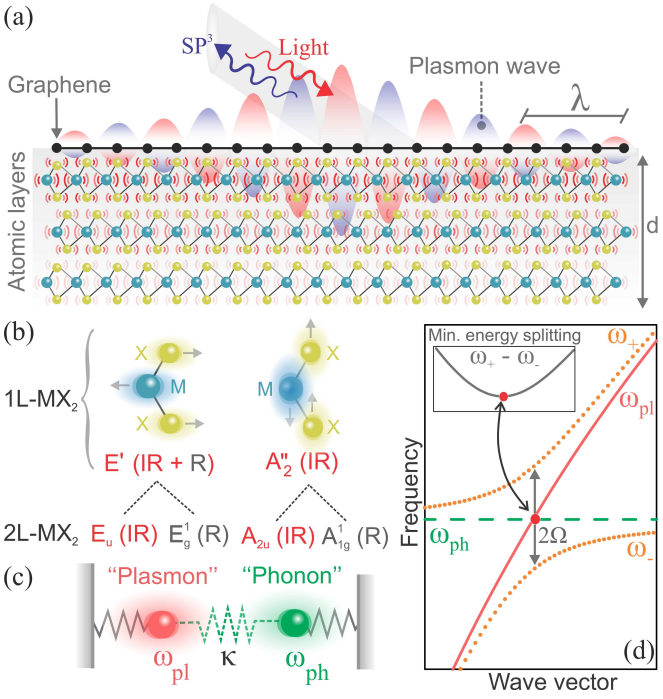

FIG. 1. (Color online) (a) Schematic illustration of the Dirac plasmon wave and the phonon-polariton vibration in van der Waals heterostructures (vdWh) composed by a monolayer graphene (G) on 3-MX_2 (M=W, Mo and X=S, Se). The graphene surface plasmon-phonon polariton wavelength is λ. Note that the monolayer graphene covers the entire sample. The hybridization of the phonon-polariton vibration in a vdWh with the Dirac plasmon originates from the hybridized surface plasmons (SP_3). (b) (Top) Representation of the in-plane E′ (IR and R), and out-of-plane A_2'' (IR), optical phonon vibrations for a monolayer of TMDs (1L-MX_2). (Bottom) For an even number of layers, these E′ and A_2'' modes split into E_u (IR) and E_g^1 (R), and A_{2u} (IR) and A_{1g}^1 (R), respectively. (c) Plasmon and phonon coupling pictorially depicted as two coupled classical mechanical oscillators. The strength of the coupling is determined by κ and gives rise to a splitting in the two eigenfrequencies ω_{ph} and ω_{pl}. (d) Qualitative representation of the eigenfrequencies ω_{ph} (horizontal green dashed line) and ω_{pl} (solid red line) of the uncoupled ($\kappa = 0$) plasmon-phonon system. The modes of the coupled system are represented by the upper (ω_+) and lower (ω_-) eigenfrequencies (orange dotted lines), its difference is called minimal energy splitting (see inset). Ω quantifies the strength of the plasmon-phonon coupling.

shown in Fig. 1(d). By investigating the specific way in which the anti-crossing is manifested, one can infer the way in which hybridization occurs, quantified by the coupling strength, Ω, between Dirac plasmons and environmental phonons.

Whether hybridization is significant or not depends on the strength of the plasmon-phonon coupling when compared to other relevant energy scales, for example, the phonon energy and linewidth [55]. The latter is schematically presented in Fig. 1(d) as an orange shade along the hybrid modes. In this context, the splitting becomes only significant when the coupling Ω exceeds the linewidths of the two coupled systems, which also enables the experimental observation of these two modes. Thus, if Ω is very small compared to other important energy scales, for example, the phonon energy, the coupling is negligible and is not strong enough to change the original (uncoupled) frequencies. This defines different coupling regimes: the first one, where Ω can be neglected, is classified as "weak coupling" (WC) [55, 56]. On the other hand, if the strength of the plasmon-phonon coupling is large enough to modify the uncoupled energy spectrum, thus creating hybrid plasmon-phonon modes, the coupling regime is classified as "strong" (SC) or "ultrastrong" coupling (USC) [55–57]. The latter enables more efficient plasmon-phonon interactions, resulting in electro-optical devices with high efficiency when compared to those based on SC [58]. For the purposes of this article, we define the WC, SC and USC regimes in a pragmatic way: after obtaining Ω, we normalize the coupling strength in relation to the phonon frequency that originates the hybridization as $\eta = \Omega/\hbar\omega_{ph}$; then, we classify the system as WC, SC and USC when $\eta < 0.01$, $0.01 \leq \eta < 0.1$ and $\eta \geq 0.1$, respectively [58].

In this paper, an investigation on the coupling between Dirac plasmon and IR-active TMDs phonons is presented. Through realistic simulations at the level of density functional theory (DFT), many-body perturbation theory and the random phase approximation (RPA) [59, 60], in combination with the quantum electrostatic heterostructure model (QEH) [61], we are able to investigate the way in which the coupling between graphene plasmons and some of the IR-active phonon modes of few layer MX_2 depends on the number of heterostructure layers, define the coupling regime and, more significantly, identify how the Fermi energy contributes to maximize the coupling strength. Furthermore, the use of QEH also allows us to analyse how the properties of the environment are affected even when a single monolayer is added to the vdWhs. We show that a semi-classical theory within the RPA is capable of capturing all relevant characteristics of the SPPPs coupling taking into account the TMDs thickness up to several layers. Therefore, we provide a realistic evaluation of the way in which the investigated phonon modes of the TMDs layers couple to the electromagnetic field of the plasmon modes and describe the dependence of the coupling strength up to the bulk limit. Finally, we show how controlling the graphene Fermi energy can maximize the coupling, towards SC and USC regimes in TMDs-based vdWhs. Although the study presented here considers only hexagonal MoS_2 and WS_2, it can easily be extended to all other TMDs.

The paper is structured as follows: In Sec. II we introduce the theoretical treatment of Dirac plasmons in vdWhs, by presenting an effective dynamical non-local background dielectric function that takes into account the TMDs thickness, the semi-classical RPA-based theory and the way in which the QEH calculates the role of

each layer separately. In Sec. III, we present the results of the plasmon-phonon dispersion in the (q,ω)-plane emphasizing which phonon modes are significantly coupled to the graphene plasmons and compare the QEH results to those from the semi-classical model. Then, we show the dependence of the SPPPs coupling on the number of TMDs layers for the IR-active in-plane (E') and out-of-plane (A_2'') phonon modes, highlighting which of them are in WC, SC, or USC regimes, through the normalization of the coupling η. By the end of Sec. III, we discuss how the Fermi energy affects the plasmon-phonon coupling and, finally, in Sec. IV, we present our conclusions.

II. PLASMON-PHONON-POLARITONS AND HYBRID MODES

Dirac plasmons, density oscillations of Dirac fermions in graphene, can be obtained from the total system's dielectric function $\epsilon(q,\omega)$ within the random phase approximation (RPA) [28, 62]. To do so, we find the solution of the plasmon equation which corresponds to the zeroes of $\epsilon(q,\omega)$ taking [28, 29, 62–65]

$$\epsilon(q,\omega) = 1 - v(q,\omega)\tilde{\chi}_{\rm nn}(q,\omega) = 0 \ , \tag{1}$$

where $v\,(q,\omega)$ is the Fourier transform of the Coulomb interaction between the Dirac electrons and $\tilde{\chi}_{\rm nn}(q,\omega)$ is the proper density-density response function [28]. In general, both functions depend on the properties of the system as a whole. Nevertheless, within the RPA, we can approximate $\tilde{\chi}_{\rm nn}(q,\omega)$ by the non-interacting density-density response function of a 2D massless Dirac fermion $\chi^0(q,\omega)$, which depends only on the properties of graphene [63–65]. On the other hand, $v\,(q,\omega)$ describes the electromagnetic field lines that mainly propagate through the surrounding of the graphene sheet, and are, therefore, strongly affected by them. In general, the 2D Fourier transform of the electron-electron Coulomb interaction is defined as

$$v(q,\omega) = \frac{2\pi e^2}{q\epsilon_{\rm env}(q,d)} \ . \tag{2}$$

As one can see from Eq. (2), it is the screening of the Coulomb interaction introduced by the effective dynamical background dielectric function $\epsilon_{\rm env}(q)$ that encodes the presence of the environment. To include the contribution of the TMDs thickness d (see Fig. 1(a)) to the screening, we define the background dielectric function as [66]

$$\epsilon_{\rm env}(q,d) = \left(\frac{2}{\epsilon_a+\epsilon_b}\frac{\sqrt{\epsilon_x(d)\epsilon_z(d)}+\epsilon_b\,\xi(d)}{\sqrt{\epsilon_x(d)\epsilon_z(d)}+\tilde{\epsilon}\,\xi(d)}\right)^{-1} \ . \tag{3}$$

In Eq. (3), we have $\xi(d) = \tanh(qd\sqrt{\epsilon_x(d)/\epsilon_z(d)}$ and $\tilde{\varepsilon} = (\epsilon_x(d)\epsilon_z(d)+\epsilon_a\epsilon_b)/\,(\epsilon_a+\epsilon_b)$. $\epsilon_{a,b}=1$ is the dielectric constant of the vacuum above and below the 2D materials slab. $\epsilon_x(d)$ and $\epsilon_z(d)$ are, respectively, the static in-plane and out-of-plane dielectric constants of the TMDs, where we have modified the notation to explicitly indicate its dependence on the TMDs thickness [67, 68]. In order to facilitate the understanding of how plasmons couple with phonons, giving rise to hybrid modes, we assume that the plasmon dispersion attains its long-wavelength form, [41, 63, 64]

$$\hbar\omega_{pl} = \sqrt{\frac{\alpha_{ee}N_F\hbar v_F}{2}\frac{E_F q}{\epsilon_{\rm env}(q,d)}} \ . \tag{4}$$

In Eq. (4), $\alpha_{\rm ee} = 2.2$, $N_F = 4$ and $v_{\rm F} = 10^6$ m/s are parameters related to the graphene sheet corresponding to the graphene fine structure constant, the number of Fermion flavours and the Fermi velocity, respectively [18]. $E_{\rm F}$ is the Fermi level of graphene.

A. Coupling Dirac plasmon to phonons polaritons

To introduce the concept of plasmon-phonon coupling, the simple classical analogy with two coupled harmonic oscillators, pictorially represented in Fig. 1(c) with "plasmon" and "phonon" representing the masses a and b, respectively, is commonly used [54, 55]. When $\kappa \neq 0$ the two oscillators interact with each other, forming a unique system, with hybridized eigenfrequencies [53]. Due to this hybridization, an anticrossing of dispersion curves is formed, resulting in a coupling strength [53]:

$$2\Omega = \frac{\kappa}{\sqrt{m_a\omega_a m_b\omega_b}} \ . \tag{5}$$

In the context of SPPPs, the coupling is similar to this classical point of view: when Dirac plasmons couple to the TMDs IR-active phonons, a hybridization occurs at $\omega_{\rm pl} = \omega_{\rm ph}$, giving rise to an anticrossing in the SPPPs dispersion for frequencies close to the phonon frequency, as presented in Fig. 1(d). For frequencies further away from the phonon frequency, the original energy remains practically unchanged from the uncoupled case. In other words, the uncoupled phonon ($\omega_{\rm ph}$) and graphene plasmon ($\omega_{\rm pl}$) frequencies, represented in Fig. 1(d) as a horizontal green dashed and a solid red ($\propto \sqrt{q}$) lines, respectively, presents hybrid modes (ω_+ and ω_-) close the phonon frequency when coupled.

To quantify the SPPPs coupling (Ω), we start from its Hamiltonian, defined as [69]

$$H = H_{\rm pl} + H_{\rm ph} + H_{\rm pl-ph} \ . \tag{6}$$

Here, $H_{\rm pl}$ is the Hamiltonian for the plasmons in the absence of the coupling to the phonons $H_{\rm ph}$, while $H_{\rm pl-ph}$ describes the coupling between them. In second quantization notation, this yields [69]

$$H = \hbar[\omega_{\rm pl}\hat{a}^\dagger_{\mathbf{q}}\hat{a}_{\mathbf{q}} + \omega_{\rm ph}\hat{b}^\dagger_{\mathbf{q}}\hat{b}_{\mathbf{q}} + \Omega_{\mathbf{q}}(\hat{a}^\dagger_{\mathbf{q}} + \hat{a}_{-\mathbf{q}})(\hat{b}^\dagger_{-\mathbf{q}} + \hat{b}_{\mathbf{q}})] \ , \tag{7}$$

where $\hat{a}^\dagger_{\mathbf{q}}$ and $\hat{a}_{\mathbf{q}}$ are creation and annihilation operators, respectively, for a Dirac plasmon (SP^2) with frequency

TABLE I. Optical phonon frequencies for the free-standing monolayer of MoS_2 and WS_2 considered from the QEH calculations. Their vibrational optical phonon modes of a single monolayer are represented by E″ (R), E′ (IR and R), A_1' (R) and A_2'' (IR), where IR (R) means that the mode is active for infrared (Raman) excitations [42, 70–74].

	Phonon frequencies (meV)			
	1 (E″)	2 (E′)	3 (A_1')	4 (A_2'')
MoS_2	34.19	46.35	47.59	56.16
WS_2	35.56	42.85	50.12	51.00

$\hbar\omega_{\rm pl}$ given by Eq. (4), and wave vector $\mathbf{q}$. $\hat{b}^\dagger_{\mathbf{q}}$ and $\hat{b}_{\mathbf{q}}$ are those for the collective vibration modes with energy $\hbar\omega_{\rm ph}$ (taken as a constant, as presented in Tab. I). In Eq. (7), $\Omega_{\mathbf{q}}$ plays the role of the coupling energy associated with the interaction between phonons and the Dirac plasmon. Consequently, the eigenfrequencies are obtained taking $\det[H] = 0$, resulting in [69]

$$\omega_\pm^2 = \frac{1}{2}\left[\omega_{\rm ph}^2 + \omega_{\rm pl}^2 \pm \sqrt{(\omega_{\rm ph}^2 - \omega_{\rm pl}^2)^2 + 4\Omega^2\omega_{\rm ph}\omega_{\rm pl}}\,\right]. \quad (8)$$

Equation (8) is similar to those obtained from a classical system formed by two coupled oscillators [53, 54], where the coupling Ω arises due to the hybridization between two (quasi)-particles, as shown in Fig. 1(d).

The goal of the current study is to identify the coupling strength Ω from realistic calculations of the anticrossing between plasmon and phonon branches. From Eq. (8), one finds that Ω can be calculated in two ways: on the one hand, one can find the minimum of the energy difference between the two branches, i.e. $\Omega_{\rm min} = \min_q(\omega_+(q) - \omega_-(q))$ (see Fig. 1(d)). On the other hand, it can also be calculated at the crossing point of the phonon frequency with the unperturbed plasmon. Here, the coupling strength corresponds to the energy difference between the two branches evaluated at the wave vector $q_{\rm pl}(\omega_{\rm ph})$, i.e. $\Omega_{\rm cp} = \omega_+(q_{\rm pl}) - \omega_-(q_{\rm pl})$. Note that in the case of a system consisting of a single plasmon and phonon, both methods are equivalent, because in that case Eq. (7) corresponds to the full system. However, once multiple phonons start to interfere with the plasmon, the model is only approximately correct and both methods will not yield the same result. In order to quantify the plasmon-phonon interaction also in the presence of multiple phonons, we always evaluate Ω using both methods. If the difference between both methods is large with respect to the nominal value of the coupling, i.e. if $\Delta\Omega = |\Omega_{\rm cp} - \Omega_{min}| \sim \Omega_i$, a hierarchy is necessary. For example, in the case where there are two relevant phonon modes, as discussed in the succeeding examples of this work, we find that it is necessary to calculate $\Omega_{\rm min}$ for the smallest value, while $\Omega_{\rm cp}$ is needed for the strongest coupling. This is because, in that case, the plasmon-phonon coupling becomes of the order of the frequency difference between the two involved phonon modes.

B. Quantum electrostatic heterostructure

In order to obtain realistic results for the plasmon-phonon coupling, we used the quantum-electrostatic heterostructure (QEH) model [61], a computational DFT-based method which includes screening from electronic transitions at the level of the random phase approximation (RPA).

More recently, the QEH model received an implementation to take into account contributions to the dielectric function of active phonons in the 2D layers, screening from homogeneous bulk substrates, and doping contributions of graphene and of a vast number of different TMDs [60, 75]. The model is especially suited for the current investigation because it calculates the total dielectric properties of the vdWhs in which the contribution of each layer is treated separately and has been demonstrated to be a very useful tool for the study of plasmons in different heterostructures [60, 75–78]. For example, in Ref. [76], the authors employ the QEH method to investigate the possibility of probing the structure and composition of different vdWhs made by a monolayer graphene on top of different TMDs, by means of the sensitivity of the graphene plasmons to the dielectric environment. Also, in Ref. [76], QEH results were compared to (i) experimental results for heterostructures composed by graphene and hexagonal boron nitride (hBN), as well as to (ii) random phase approximation (RPA) calculations for graphene on top of silicon dioxide (SiO_2), where great agreement is verified in both cases.

One of the major advantages of the use of the QEH model is the availability of a vast database containing the dielectric building blocks (DBBs) of 2D materials [79]. This gives us the possibility to reuse previously obtained DFT results, allowing a careful analysis of the plasmon-phonon coupling in different vdWh systems on a layer-by-layer basis, without the need to treat the dielectric environment as slabs of bulk material.

For completeness, we summarize, as a following, the main idea behind QEH calculations. For a step-by-step explanation, see Refs. [61] and [60] and their respective Supplemental Materials.

Loss function and plasmon dispersion

In a few words, the QEH numerically couples the density-density response function of each i-th layer $\chi_i\left(z, z', \mathbf{q}_\parallel, \omega\right)$, present in the DBBs that were previously obtained through *ab-initio* calculations. The total response function of the entire vdWhs is built by coupling each single layer together, i.e. the DDBs, using the long-range Coulomb interaction by solving a Dyson-like equation. Thereby, the Dyson equation of the total density-density response function of the complete vdWh

reads [61]

$$\chi_{i\alpha,j\beta} = \chi_{i\alpha}\delta_{i\alpha,j\beta} + \chi_{i\alpha}\sum_{k\neq i,\gamma} V_{i\alpha,k\gamma}\chi_{k\gamma,j\beta} \ , \tag{9}$$

where, for simplicity, the $\mathbf{q}_\parallel$ and ω variables were omitted. In Eq. (9), $\alpha = 0, 1$ represents the monopole and dipole components, respectively, and the Coulomb matrices are defined as

$$V_{i\alpha,k\gamma}\left(\mathbf{q}_\parallel\right) = \int \rho_{i\alpha}\left(z,\mathbf{q}_\parallel\right)\Phi_{k\gamma}\left(z,\mathbf{q}_\parallel\right)dz \ , \tag{10}$$

where $\Phi_{k\gamma}\left(z,\mathbf{q}_\parallel\right)$ is the potential created by the density profile, $\rho_{k\gamma}\left(z,\mathbf{q}_\parallel\right)$.

Through this formalism, one obtains the inverse dielectric function of the vdWh as

$$\epsilon^{-1}_{i\alpha,j\beta}\left(\mathbf{q}_\parallel,\omega\right) = \delta_{i\alpha,j\beta} + \sum_{k\gamma} V_{i\alpha,j\beta}\left(\mathbf{q}_\parallel\right)\chi_{k\gamma,j\beta}\left(\mathbf{q}_\parallel,\omega\right) \ . \tag{11}$$

Notice that in contrast to the dielectric function presented in Eq. (1), here we obtain a tensorial form. Consequently, the loss function can be found through

$$L\left(\mathbf{q}_\parallel,\omega\right) = -\mathrm{Im}\left[\mathrm{Tr}\left(\epsilon^{-1}\left(\mathbf{q}_\parallel,\omega\right)\right)\right] \ . \tag{12}$$

Finally, collective modes, such as the plasmon dispersion, can now be found as the maxima of the loss function, Eq. (12).

Lattice polarizability and phonon contribution

The phonon contribution of the isolated 2D material, that originates nontrivial effects in the (q,ω)-dispersion when coupled to surface plasmon-polaritons, giving rise to SPPPs, is obtained through the Born effective charges and Γ-point phonon modes of the individually layers [60]. The Born effective charges are defined as tensors that give the proportionality between the variation of the 2D polarization density P_i, due to an atomic displacement, and it is defined as [60]

$$Z_{i,aj} = \frac{\mathrm{A_{cell}}}{e}\left.\frac{\partial P_i}{\partial u_{\mathrm{aj}}}\right|_{E=0} \ , \tag{13}$$

where $\mathrm{A_{cell}}$ is the in-plane area of the 2D layer, a denotes an atom, and ij are cartesian coordinates.

Subsequently, the lattice polarizability of a 2D material in the optical limit ($\mathbf{q} = 0$) can be obtained through [60]:

$$\alpha^{\mathrm{lat}}_{ij}(\omega) = \frac{e^2}{\mathrm{A_{cell}}}\sum_{ak,bl} Z_{i,ak}[(\mathbf{C} - \mathbf{M}(\omega^2 - i\gamma\omega))^{-1}]_{ak,bl}Z_{j,bl} \ , \tag{14}$$

where $\mathbf{C}$ is the force constant matrix in the optical limit, $\mathbf{M}$ is a diagonal matrix containing the atomic masses, and γ is a relaxation rate (see appendix of Ref .[60] for a derivation of Eq. 14).

Thus, considering the contributions of electrons and phonons, the total monopole and dipole component of the DBB of layer i are defined as

$$\chi^{\mathrm{total}}_{i0}\left(\mathbf{q}_\parallel,\omega\right) = \chi^{\mathrm{el}}_{i0}\left(\mathbf{q}_\parallel,\omega\right) - \mathbf{q}^2_\parallel\alpha^{\mathrm{lat}}_\parallel\left(\omega\right) \tag{15a}$$

$$\chi^{\mathrm{total}}_{i1}\left(\mathbf{q}_\parallel,\omega\right) = \chi^{\mathrm{el}}_{i1}\left(\mathbf{q}_\parallel,\omega\right) - \alpha^{\mathrm{lat}}_{zz}\left(\omega\right) \ , \tag{15b}$$

where $\alpha^{\mathrm{lat}}_\parallel$ denotes the 2×2 in-plane submatrix of α^{lat}. The total response functions are then used in Eq. (9), from which the consecutive loss function is obtained.

III. STRENGTH OF PLASMON-PHONON COUPLING IN VAN DER WAALS HETEROSTRUCTURES

TMDs are slightly polar materials, i.e their crystalline structure contains atoms with different electronegativities, consequently, certain IR-active phonon modes at the Γ-point give rise to a macroscopic electric field [71, 80]. Optical phonon modes can be labelled in terms of their irreducible representations. At the Γ-point, the phonon modes of MoS_2 and WS_2 with an odd number of layers are E″ (R), E′ (IR and R), A'_1 (R) and A''_2 (IR), while A_{1g} (R), A_{2u} (IR), E_g (R) and E_u (IR) are the modes for even number of TMDs layers [42]. Appendix A provides a description of the optical activity of phonon modes at Γ-point of 2H-TMDs.

In Fig. 2(a), we present the plasmon dispersion of SP^2 modes, i.e Dirac plasmons with the surrounding polarization cloud [41, 80], but disregarding the TMDs phonon vibrations, at the Fermi energy given by $E_F = 100$ meV, for a G/N-MoS_2 vdWhs, with $N = 1$, 10 and 20 TMD layers. In this case, to turn off the phonon contribution, the QEH calculation is performed taking into account only the in-plane high-frequency dielectric constant of individual layers at the optical limit $\epsilon^\infty_\parallel$. The loss functions obtained by the QEH calculation, shown as a color map for $N = 10$, are in accordance with Eq. (4), whose results are represented by white dashed curves in Fig. 2(a). As the number of layers increases, q increases for a fixed frequency in the plasmon dispersion, since the total dielectric function of the environment $\epsilon_{\mathrm{env}}(q,d)$ also increases, since the screening is proportional to the number of layers. This is verified by the solid and dashed-dotted lines in Fig. 2(a), which represent the maxima of the loss function for $N = 1$ and 20, respectively. When phonon contributions are taken into account, as shown in Fig. 2(b), anticrossings in the SP^2 dispersion arise close to the regions where $\omega_{\mathrm{pl}} = \omega_{\mathrm{ph}}$. Although monolayer MoS_2 has four non-degenerate optical phonon modes, only two of them are IR-active, as mentioned earlier, giving rise to significant hybrid modes. As the number of layer increases, each of these phonon modes splits into more modes, due to inter-layer interactions. However, the QEH method employed here resort to electrostatic coupling between the layers, which requires the investigated phonon modes

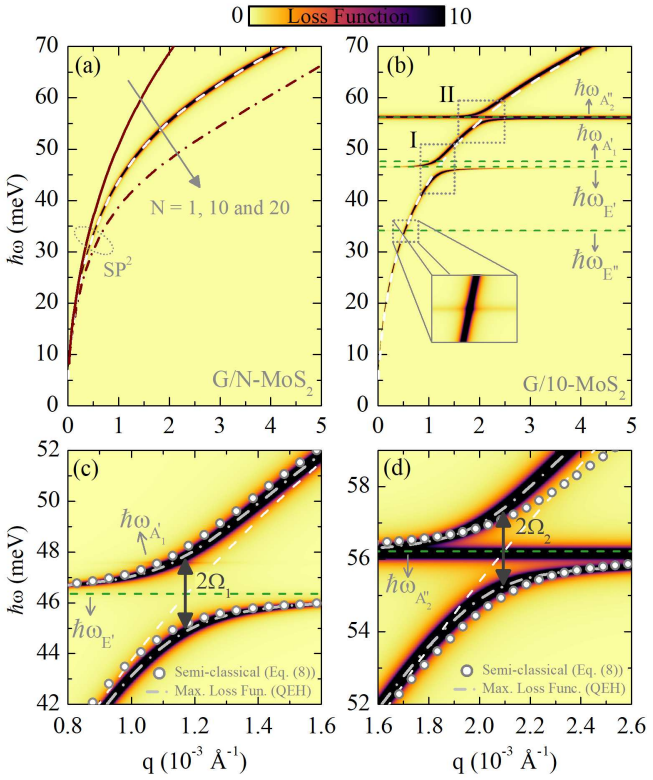

FIG. 2. (Color online) (a) Plasmon dispersion of the SP^2 for G/N-MoS_2 with N=1 (solid), 10 (white dashed) and 20 (dashed-dotted) at $E_F = 100$ meV obtained from the QEH without plasmon-phonon coupling ($\Omega = 0$). The loss function is shown as a color map for $N = 10$. (b) SPPPs dispersion for G/10-MoS_2 with $E_F = 100$ meV. The regions with IR-active phonons modes, namely E′ and A_2'', that hybridize with the Dirac plasmons giving rise to anti-crossings in the eigenfrequencies when $\omega_{pl} = \omega_{ph}$, are highlighted by the rectangles I and II. The magnification emphasizes the lack of coupling between Dirac plasmons and the E″ phonon mode, which is Raman-active, as well as the absence of the split phonon modes expected for such multilayer TMD. This prevents us from properly studying plasmon-phonon couplings with this specific phonon mode, or with phonon modes originating from its splitting in a multilayer system

. Horizontal green dashed lines represents the phonon frequencies of a single MoS_2 layer. (see Tab. I). (c) and (d) are magnifications of regions I and II of panel (b), around the anticrossings and close to the IR-active E′ and A_2'' phonon modes, with frequencies $\hbar\omega_{E'}$ and $\hbar\omega_{A_2''}$, respectively. $\Omega_{1(2)}$ represents the coupling strength between Dirac plasmon and IR-active in-plane (out-of-plane) vibrational phonon mode. Symbols are the eigenfrequencies obtained from the semi-classical model, Eq. (8). Dashed-doted gray lines are the maxima in the loss function, while the dashed white line is the SP^2 dispersion for reference.

to be IR-active in order to have their splitting detected by our calculations. As a consequence, even though we know the monolayer modes E'' and A_1' should also undergo a splitting in multi-layer systems, from which even IR-active modes may result, our calculations cannot detect this splitting and, therefore, the coupling between Dirac plasmons and these specific phonon modes cannot be properly investigated here. For similar reasons, the proposed method cannot detect the low-frequency (≈ 5 meV) shear/breathing phonon modes of multilayer TMDs.[81–83] We therefore rather focus all our attention on the study of plasmon-phonon couplings and their hybrid SPPPs states with the E′, E_u, A_2'', and A_{2u} phonon modes, whose splitting in TMDs multilayers is properly detected by the method employed here.

These SPPPs modes are presented in Figs. 2(c)-(d) as a magnification of the two square boxes highlighted in Fig. 2(b). The coupling strength between the Dirac plasmons and the in-plane E′ or E_u (out-of-plane A_2'' or A_{2u}) phonon mode is defined as Ω_1 (Ω_2). In panels (c) and (d), the symbols refer to the hybrid eigenfrequencies obtained from Eq. (8).

A. The influence of the number of TMDs layers

Using the QEH, we show in Fig. 3(a)-(d) the evolution of the SPPPs coupling strength ($\Omega_{1(2)}$) as a function of the number of layers for a vdWhs composed by MLG on top of N-MoS_2 (blue symbols and lines) and N-WS_2 (orange symbols and lines). As the number of layers increase, the SPPPs coupling ($\Omega_{1(2)}$) also increases, since more oscillators are involved, i.e more phonons are available to couple with the Dirac plasmons [84, 85]. For a few TMD layers ($N < 10$), there are two important and peculiar aspects to be considered in here: (i) the $\sqrt{N}$ behavior of Ω_1, that is the coupling between plasmon and in-plane phonon modes, Fig. 3(b), and (ii) the linear dependence of the out-of-plane phonon coupling Ω_2, Fig. 3(d). To explain this behaviour, we analyse the effective dielectric function [84, 86]

$$\epsilon_i^{\text{eff}} \approx \epsilon_{\text{env}} \left(1 - \frac{\omega_{pl}^2}{\omega^2} - \frac{M_i \delta_i^2}{\omega^2 - \omega_{\text{ph},i}^2 + \delta_i^2} \right) . \qquad (16)$$

For simplicity, but without loss of generality, in Eq. (16), $i = 1$ ($i = 2$) describes an effective coupling of Dirac plasmon and the E′ (odd number of layers) or E_u (even number of layers) (A_2'' (odd number of layers) or A_{2u} (even number of layers)) TMD phonon mode. Notice that E′ /E_u and A_2'' A_{2u} phonons exhibit different geometric properties. The former two are in-plane modes, for which M_1 increase linearly with the number of layers N. Conversely, the latter two are out-of-plane modes, with M_2 scaling with N^2 instead. In Eq. (16), δ_i is the coupling between the phonon mode E′ (A_2'') in a single TMD layer and the Dirac plasmon, i.e. it is the smallest plasmon-phonon coupling strength possible for the system. Notice that this approximation only holds as long as the penetration depth of the plasmon mode is larger than the TMD thickness. In this case, the zeroes of Eq. (16)

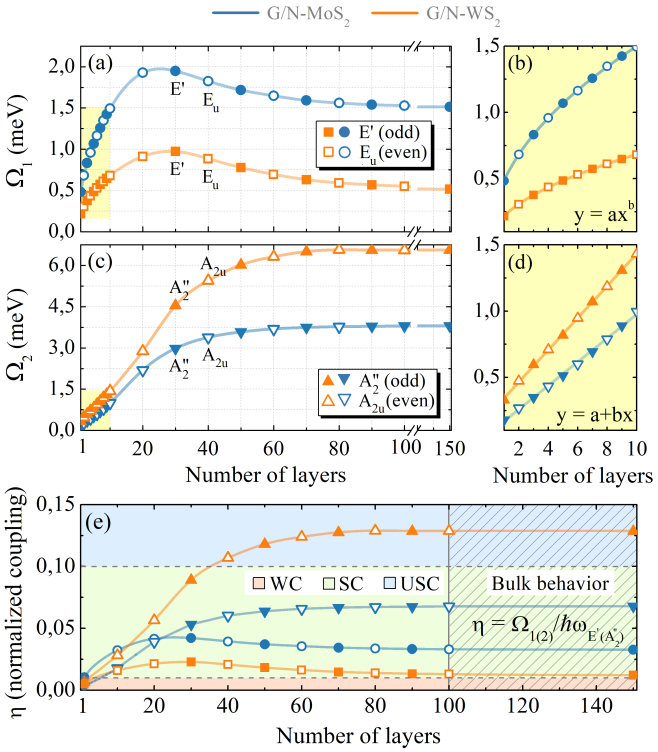

FIG. 3. (Color online) SPPPs coupling strength ($\Omega_{1(2)}$) as a function of the number of TMDs layers for graphene at $E_F = 100$ meV on top of N-MoS_2 (blue lines and circles) and N-WS_2 (orange lines and circles). (a) Coupling energy between Dirac plasmon and the IR-active in-plane E′ (solid symbols) and E_u (open symbols) phonon modes, for odd and even number of layers, respectively. (b) Magnification of the results in (a) from 1 to 10 layers (yellow region), emphasizing that $\Omega_1 \propto \sqrt{N}$. (c) The same as in (a), but now for the coupling strength Ω_2, i.e considering the IR-active out-of-plane A_2'' (solid symbols) and A_{2u} (open symbols) phonon modes, for odd and even number of layers, respectively. (d) Magnification in panel (c) from 1 to 10 layers (yellow region), emphasizing that $\Omega_2 \propto N$. (e) SPPPs coupling strength normalized in relation to their respective monolayer phonon frequencies defined as $\eta = \Omega_{1(2)}/\hbar\omega_{E'(A_2'')}$. Three different regions, blue, green and pink, represent the WC ($\eta < 0.01$), SC ($0.01 \leq \eta < 0.1$) and USC ($\eta \geq 0.1$), respectively [58]. The hatched area represents the bulk limit of the SPPPs coupling, reached for approximately 100 TMDs layers.

yield the relation between the hybrid modes as [84]

$$\omega_i^{\pm} \approx \omega_{\mathrm{ph},i} \pm \frac{1}{2}\sqrt{M_i}\delta_i \ . \tag{17}$$

Therefore, Eq. (17) reveals that, within this model, the SPPPs coupling $\Omega_{1(2)}$, given as $\Omega_i = \omega_i^+ - \omega_i^-$, is indeed expected to depend on the number of layers N as $\Omega_1 = \sqrt{M_1}\delta_1 = \sqrt{N}\delta_1$ and $\Omega_2 = \sqrt{M_2}\delta_2 = N\delta_2$.

B. SPPPs interaction: weak, strong and ultra-strong coupling regime

Based on the fact that the transverse (TO) and longitudinal (LO) optical splitting in MX_2 is very small, due to the plasmon-phonon coupling, [87, 88], we define the normalized parameter $\eta = \Omega_{1(2)}/\hbar\omega_{E'(A_2'')}$, where, in this case, $\omega_{E'(A_2'')}$ are phonon frequencies of a single TMD layer, as a way to quantify the coupling strength [58]. It is important to mention that, in other systems, such as nanocavities, the normalized coupling is rather taken with respect to the mid-gap between the TO and LO phonon modes, due their considerable splitting [89]. Figure 3(e) shows the normalized SPPPs coupling η as a function of the number of N-MoS_2 and N-WS_2 layers. Three different regions, blue, green and pink, represent the WC ($\eta < 0.01$), SC ($0.01 \leq \eta < 0.1$) and USC ($\eta \geq 0.1$) regimes, respectively [58]. A remarkable result is obtained for the coupling between Dirac plasmons and the IR-active out-of-plane WS_2 phonon mode, where we observe that they reach the USC regime, as illustrated in Fig. 3(e) by orange triangles. Furthermore, for $N > 100$ all results remain unchanged, showing that the bulk behavior was reached for 100 TMD layers or more (see hatched area in Fig. 3(e)).

To illustrate the WC, SC and USC regime in a TMDs-based vdWhs, we shown in Fig. 4 an overview of SPPPs dispersion in the (q,ω)-plane through the color maps of the loss function, defined by Eq. (12), and the loss spectra for a fixed q at the point were the SPPPs coupling $\Omega_{1(2)}$ were calculated. As expected, for a MLG on top of 1-MoS_2 or 1-WS_2, Figs. 4(a) and 4(c), respectively, the SPPPs coupling are in the WC regime. In this case, the modes that compose the anticrossing, arising due their hybridization, are practically indistinguishable, as compared to the line width of the non-coupled modes. The loss spectra below each panel emphasizes how weak this couplings is, since the peaks, represented by blue (purple) arrows for Ω_1 (Ω_2), are very close to each other, presenting a normalized coupling η less than 0.01. In Fig. 4(b), both Ω_1 and Ω_2 are in the SC, presenting a well defined anticrossing and a loss spectra with well separated peaks, where η is given by 0.047 and 0.063, respectively. Finally, although Ω_1 in Fig. 4(d) presents a SC, with $\eta = 0.18$, Ω_2 is in the USC coupling regime with $\eta = 0.12$ in this case.

C. Tuning the SPPPs coupling strength through the Fermi energy

Figure 5 shows how the Fermi energy can be use to tune the SPPPs coupling, as to maximize the plasmon-phonon interaction. In Fig. 5(a), we present the SPPPs dispersion for a vdWhs made by G/25-MoS_2 for three different values of the Fermi energy (in units of the phonon energy $\hbar\omega_{E'}$ in a single layer, see Tab. I): $E_F^A = 1\hbar\omega_{E'}$, $E_F^B = 2.3\hbar\omega_{E'}$ and $E_F^C = 3.8\hbar\omega_{E'}$, represented by the

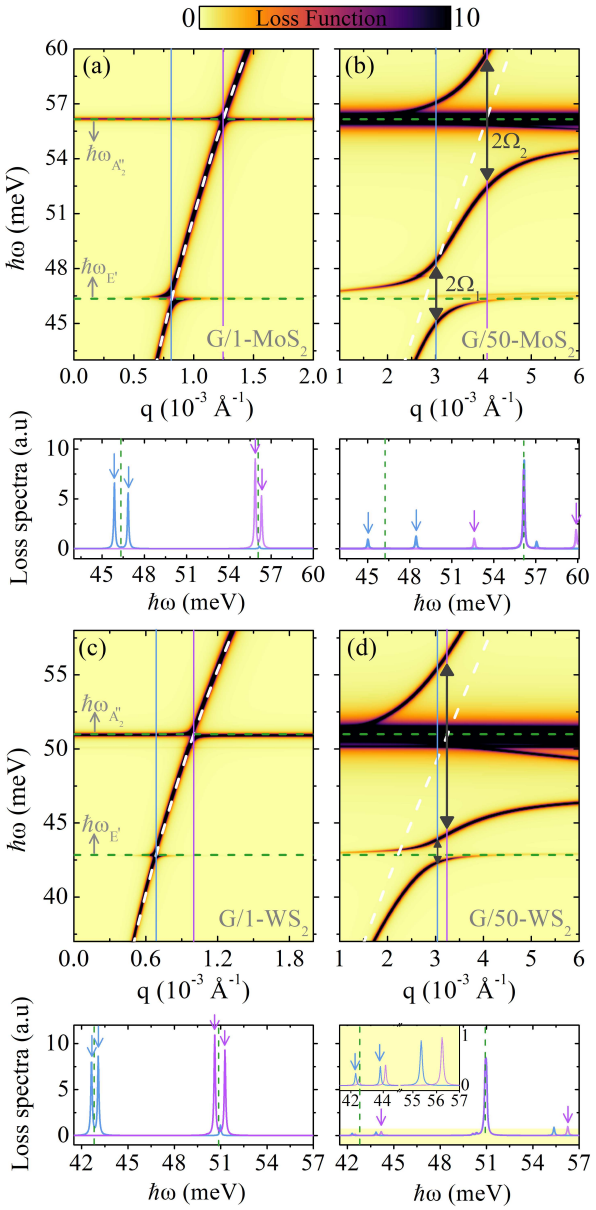

FIG. 4. (Color online) Overview of SPPPs dispersion in the (q,ω)-plane through the loss function for a MLG, at $E_F = 100$ meV, on top of (a) 1 and (b) 50 MoS_2, and on top of (c) 1 and (d) 50 WS_2. Ω_1 (Ω_2) corresponds to the coupling strength between Dirac plasmons and the IR-active in-plane E′ (out-of-plane A_2'') phonon mode. The horizontal green curves correspond to the uncoupled phonon modes calculated for a monolayer of each correspondent TMD (see Tab. I for the corespondent phonon frequencies $\hbar\omega_{E'}$ and $\hbar\omega_{A_2''}$). The uncoupled SP^2 plasmons are represented by white dashed lines, for reference. The results in each bottom panel are the loss spectra for a fixed q at the point were the SPPPs coupling strengths $\Omega_{1(2)}$ were calculated. In the bottom panel (d), a magnification of the loss spectra is shown as inset.

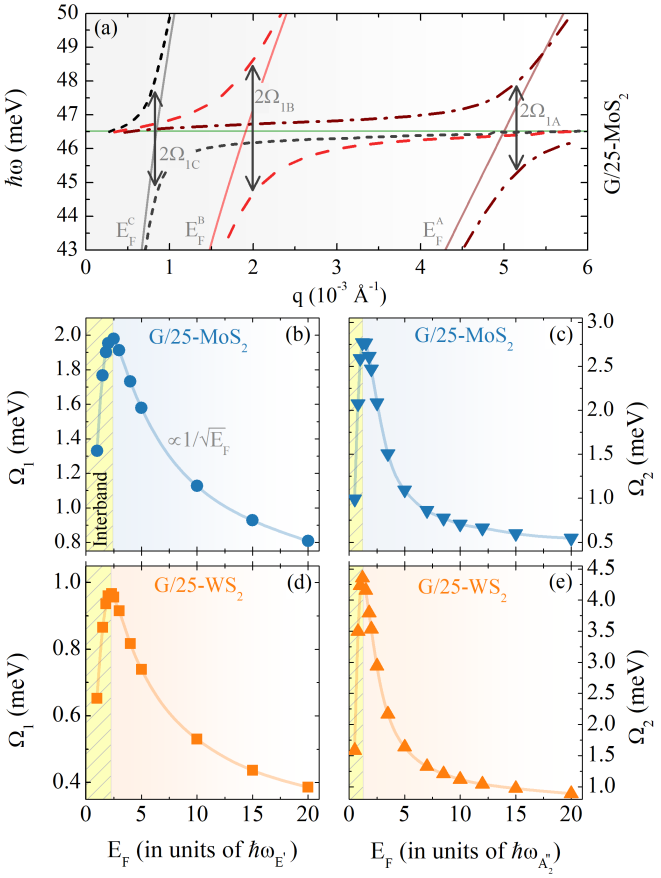

FIG. 5. (Color online) Tuning the plasmon-phonon coupling strength $\Omega_{1(2)}$ by changing the Fermi energy (in units of the corresponding phonon frequency). (a) Plasmonic dispersion of G/25-MoS_2 for different values of the Fermi energy (in units of $\hbar\omega_{E'}$) given by $E_F^A = 1\hbar\omega_{E'}$, $E_F^B = 2.3\hbar\omega_{E'}$ and $E_F^C = 3.8\hbar\omega_{E'}$. The uncoupled phonon state corresponds to the horizontal solid green line and the SP_2 plasmons are represented by the square root ($\propto \sqrt{q}$) solid lines, for reference. The SPPPs couplings (b)-(c) Ω_1 and (d)-(e) Ω_2 are shown as a function of the Fermi energy for G/25-MoS_2. The yellow region in (b)-(e) represents the interband regime, where the plasmon dispersion is damped. After that, $\Omega_{1(2)} \propto 1/\sqrt{E_F}$, i.e the Fermi energy is large enough to keep the plasmon-phonon dispersion in the long-wavelength limit, keeping the plasmonic dispersion below the interband region.

black dotted, red dashed and brown dash-dotted lines, respectively. The horizontal green line is the phonon frequency and the other solid lines are the SP_2 dispersion for reference. Fig. 5(a) shows that there is a Fermi energy value that maximizes the SPPPs coupling strength. To explain this, we show in Figs. 5(b)-(e) the SPPPs coupling parameters Ω_1 and Ω_2 as a function of the Fermi energy. In all situations, Ω_1 and Ω_2 increase until they reach a maximum value, and then they decrease with E_F, exhibiting $\propto 1/\sqrt{E_F}$ dependence.

To explain this behaviour, we identify two different coupling mechanisms that depend on the Fermi energy E_F. If the E_F is large, due to Pauli blocking, single-particle inter-band processes are suppressed. In that case, the Dirac liquid effectively behaves as a liquid of Fermions with a mass equal to the cyclotron mass

$m_c = 2E_F/v_F^2$ [18]. Equation (5) shows that in this case the plasmon-phonon coupling Ω is expected to decrease as $1/\sqrt{E_F}$. That is, because of the Dirac-like spectrum of low energy electrons in graphene, the inertial mass, corresponding to the cyclotron mass, is tunable via the Fermi level. One verifies in Eq. (5) that when two oscillators are coupled, their effective anti-crossing depends on the mass and, consequently, the coupling in our system is also expected to be tunable by the Fermi level. However, when the Fermi energy is small, Pauli blocking is lifted and inter-band single-particle processes are allowed [8, 41]. This strongly inhibits plasmon lifetime and, therefore, suppresses plasmon-phonon coupling.

Note that, for the vdWhs considered in Figs. 5(b)-(e), both SPPPs coupling Ω_1 and Ω_2 are in the SC regime. However, controlling the Fermi energy and increasing the number of layers it is possible to go from the SC to even the USC regime. The latter can be reached for Ω_2 in a MLG on top of 50 (or more) WS_2 layers, for example.

IV. CONCLUSIONS

We have demonstrated how graphene (Dirac) plasmons couple to IR-active in-plane E′ and E_u, and out-of-plane A_2'' and A_{2u} phonon modes in transition metal dichalcogenide-based van der Waals heterostructures, from few layers until the bulk limit. In order to do so, we have presented a semi-classical theory, obtained from the random phase approximation, to calculate the surface plasmon-phonon polaritons dispersion in the q-ω plane. Comparing this semi-classical theory to the results obtained through a DFT-based method, known as the quantum-electrostatic heterostructure, we have shown that the semi-classical approach provides an excellent match for many TMDs layers, capturing all relevant characteristics of the surface plasmon-phonon polaritons.

Furthermore, using the quantum-electrostatic heterostructure model, we have calculated the loss function of vdWHs composed by monolayer graphene on top of TMDs multi-layers. Our results prove that, although we have weak and strong coupling regimes in this TMDs-based vdWhs, it is also possible to achieve the ultra strong coupling regime for the coupling between Dirac plasmons and A_2''or A_{2u} for 40 or more WS_2 layers. In addition, we explain the nature of the graphene plasmons coupling to IR-active in-plane E′ and E_u, and out-of-plane A_2'' and A_{2u} phonon modes, from a few TMDs layers to the bulk behavior. Not less important, we have demonstrated the possibility of tune the SPPPs coupling strength through the graphene Fermi energy, explaining its $1/\sqrt{E_F}$ dependence. It is important to highlight that plasmons in graphene can be experimentally observed using, for example, scattering-type scanning near-field optical microscope (s-SNOM) in photocurrent mode. Therefore, using current experimental techniques, our results suggest the possibility of creating/exciting SPPPs and to study the coupling regimes discussed here for vdWhs composed by graphene and MoS_2 or WS_2.

ACKNOWLEDGMENTS

Discussions with D. J. P. de Sousa, L. S. R. Cavalcante, T. Low and K. S. Thygesen are gratefully acknowledged. This work was financially supported by the Brazilian Council for Research (CNPq), Brazilian National Council for the Improvement of Higher Education (CAPES) and by the Research Foundation Flanders (FWO), through postdoctoral fellowships granted to B.V.D and A.C.

Appendix A: A brief description of phonon modes on 2H-TMDs at Γ-point

Based on Ref. [42], this Appendix presents, for the sake of completeness, a brief description of 2H-TMDs phonon modes at the Γ-point. All phonon modes discussed here are well illustrated in Refs. [42] and [52].

The unit cell of a bulk 2H-MX_2 consists of two X-M-X layers per unit cell, presenting a total of six atoms and, consequently, 18 phonon modes (3 acoustic and 15 optical modes) [42]. Due to its D_{6h} point group symmetry, the irreducible bulk 2H-MX_2 phonon modes at Γ-point are represented by [42, 51, 52]: $\Gamma = A_{1g}+2A_{2u}+2B_{2g}+B_{1u}+E_{1g}+2E_{1u}+2E_{2g}+E_{2u}$. Here, two of them are acoustic modes (A_{2u} and E_{1u}), three are R-active (A_{1g}, E_{1g} and E_{2g}), two are IR-active (B_{2g} and E_{1u}), and finally, three of them are optically inactive, i.e. silent (B_{2g}, B_{1u} and E_{2u}) [42, 52, 90]. E-modes are doubly degenerate in xy-plane.

On the other hand, unlike bulk 2H-MX_2, few layer TMDs presents a lack of translational symmetry along the z-axis perpendicular to the basal xy-plane [42, 91]. For example, for odd number of layers, MX_2 has D_{3h} point group symmetry and, in particular, a monolayer presents nine vibrational phonon modes at the Γ-point, since the unit cell is composed of three atoms, which are represented as: $\Gamma_{odd} = 2A_2'' + A_1' + 2E' + E''$. Here, one A_2'' and one E′ are acoustic modes, another A_2'' is IR-active, A_1' and E″ are R-active, and another E′ is both R- and IR-active. In the case of even 2H-MX_2 layers, D_{3d} is the point group symmetry, due to the inversion symmetry. For the sake of simplicity, but without loss of generality, let us consider the bilayer of 2H-MX_2, for example: it has a unit cell composed of six atoms with 18 normal vibrational modes at the Γ-point, defined as: $\Gamma_{even} = 3A_{1g} + 3A_{2u} + 3E_g + 3E_u$, where one A_{2u} and one E_u are acoustic modes, the other A_{2u} and E_u are IR-active, and A_{1g} and E_g are R-active. As the number of layers N increases, inter-layer interactions break the N-fold degeneracy of the phonon modes and, consequently, all modes split around the original frequencies. This effect, known as Davydov splitting, has been investigated through Raman spectroscopy for R-active phonon modes

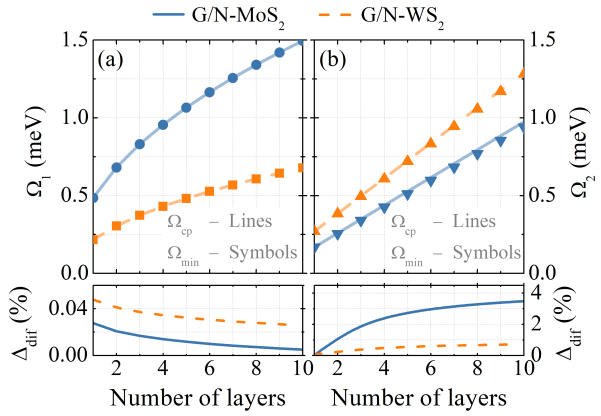

FIG. A.1. (Color online) Comparison between the SPPPs coupling strength, for few layers of TMD, obtained from the minimal energy splitting thought $\Omega_{\rm min}$ (symbols) and at the crossing point $\Omega_{\rm cp}$ (lines). (a) Results of the comparison between plasmons and in-plane E′ or E_u phonons in a vdWhs composed by G/N-MoS_2 (G/N-WS_2), blue (orange) symbols and lines, with $E_F = 100$ meV. (b) The same as in (a), but now for the coupling between plasmons and out-of-plane A_2'' or A_{2u} phonons. The bottom panels in (a) and (b) present the relative difference between both procedures, i.e $\Omega_{\rm min}$ and $\Omega_{\rm cp}$, defined as $\Delta_{\rm dif} = 100|\Omega_{\rm cp} - \Omega_{\rm min}|/\Omega_{\rm cp}$.

of multi-layers of different TMDs, such as MoS_2, $MoTe_2$ and WSe_2 [92, 93].

Finally, it is important to mention that one of the most important properties of 2H-TMDs phonon modes at Γ-point, resides in the fact that each of the nine previously described vibrational modes in 1-MX_2 layer, will split into corresponding two modes in both 2-MX_2 and bulk MX_2 [42]. For example, the E′ in 1-MX_2 layer give rise to the E_g^1 and E_u modes, which are R- and IR-active, respectively. Regarding the bulk MX_2, the E′ in 1-MX_2 layer splits into E_{2g}^1 and E_{1u}, also R- and IR-active, respectively. Here, the notation 1 and 2 in the upper right corner of the mode notation is used to represent modes with the same symmetry, such as E_{2g}^1 and E_{2g}^2.

Appendix B: Plasmon-phonon coupling strength at the minimal energy splitting and at the crossing point

Here, we provide a comparison for the SPPPs coupling strength as obtained from the minimum of the energy difference between the two branches $\Omega_{\rm min}$ and those obtained at the crossing point $\Omega_{\rm cp}$, as previously discussed in Sec. II A. Results are depicted in Fig. A.1(a), for the coupling between Dirac plasmons and IR-active in-plane E′ phonon mode (Ω_1), and in Fig. A.1(b) for Dirac plasmons and IR-active out-of-plane A_2'' phonon mode (Ω_2). Blue (orange) results in both panels are for G/N-MoS_2 (G/N-WS_2), with N from 1 to 10 TMDs layers, while symbols (lines) represents the results obtained from $\Omega_{\rm min}$ ($\Omega_{\rm cp}$). Both methods yield practically the same results. To quantify the difference between them, we show in the bottom panels the relative difference $\Delta_{\rm dif}$ between the results from both methods, defined as $\Delta_{\rm dif} = 100|\Omega_{\rm cp} - \Omega_{\rm min}|/\Omega_{\rm cp}$. For Ω_1, the bottom panel in Fig. A.1(a) shows relative differences lower than 0.1 %, while for Ω_2, in the bottom panel of Fig. A.1(b), they are less than 4 %.

[1] K. S. Novoselov, Science **306**, 666 (2004).
[2] S. Z. Butler *et al.*, ACS Nano **7**, 2898 (2013).
[3] A. K. Geim and I. V. Grigorieva, Nature **499**, 419 (2013).
[4] G. Fiori *et al.*, Nat. Nanotechnol **9**, 768 (2014).
[5] S. Manzeli *et al.*, Nat. Rev. Mater. **2**, 17033 (2017).
[6] K. S. Novoselov *et al.*, PNAS **102**, 10451 (2005).
[7] Q. H. Wang *et al.*, Nat. Nanotechnol **7**, 699 (2012).
[8] T. Low and P. Avouris, ACS Nano **8**, 1086 (2014).
[9] T. Low *et al.*, Nat. Mater **16**, 182 (2016).
[10] E. D. Ranieri, Nat. Nanotechnol **5**, 3011 (2014).
[11] D. Jariwala *et al.*, ACS Nano **8**, 1102 (2014).
[12] H. Zhang, ACS Nano **9**, 9451 (2015).
[13] L. Ju *et al.*, Nat. Nanotechnol **6**, 630 (2011).
[14] J. Chen *et al.*, Nature **487**, 77 (2012).
[15] K. F. Mak and J. Shan, Nat. Photonics **10**, 216 (2016).
[16] Z. G. Yu *et al.*, Sci. Reps **5**, 13783 (2015).
[17] K. F. Mak *et al.*, Phys. Rev. Lett. **105**, 136805 (2010).
[18] A. H. C. Neto *et al.*, Rev. Mod. Phys. **81**, 109 (2009).
[19] K. S. Novoselov *et al.*, Science **353**, aac9439 (2016).
[20] Y. Liu *et al.*, Nat. Rev. Mater. **1**, 1 (2016).
[21] Y. Gong *et al.*, Nat. Mater **13**, 1135 (2014).
[22] V. O. Özcelik *et al.*, Phys. Rev. B **94**, 035125 (2016).
[23] P. K. Sahoo *et al.*, Nature **553**, 63 (2018).
[24] X. Duan *et al.*, Nat. Nanotechnol **9**, 1024 (2014).
[25] Y. Gong *et al.*, Nano Lett. **15**, 6135 (2015).
[26] C. Huang *et al.*, Nat. Mater **13**, 1096 (2014).
[27] D. Jariwala *et al.*, Nat. Mater **16**, 170 (2016).
[28] G. V. Gabriele Giuliani, *Quantum Theory of the Electron Liquid* (Cambridge University Press, 2008).
[29] S. A. Maier, *Plasmonics: Fundamentals and Applications* (Springer-Verlag GmbH, 2007).
[30] A. N. Grigorenko, M. Polini, and K. S. Novoselov, Nat. Photonics **6**, 749 (2012).
[31] H. Yan *et al.*, Nat. Photonics **7**, 394 (2013).
[32] M. Jablan *et al.*, Phys. Rev. B **80**, 245435 (2009).
[33] Z. Fei *et al.*, Nature **487**, 82 (2012).
[34] Z. Fei *et al.*, Nano Lett. **11**, 4701 (2011).
[35] X. Cai *et al.*, Nat. Nanotechnol **9**, 814 (2014).
[36] R. Liu *et al.*, Nanoscale **5**, 5294 (2013).
[37] Y. Zhong *et al.*, J. Nanophotonics **9**, 093791 (2015).
[38] J. A. Schuller *et al.*, Nat. Mater **9**, 193 (2010).
[39] M. Polini, Science **351**, 229 (2016).
[40] P. Alonso-González *et al.*, Nat. Nanotechnol **12**, 31 (2016).

[41] P. A. D. Gonçalves and N. M. R. Peres, *An Introduction to Graphene Plasmonics* (World Scienctific, 2015).
[42] X. Zhang *et al.*, Chem. Soc. Rev. **44**, 2757 (2015).
[43] A. Splendiani *et al.*, Nano Lett. **10**, 1271 (2010).
[44] Z. Li *et al.*, ACS Nano **9**, 10158 (2015).
[45] M. B. Lundeberg *et al.*, Science **357**, 187 (2017).
[46] M. B. Lundeberg *et al.*, Nat. Mater **16**, 204 (2016).
[47] A. Woessner *et al.*, Nat. Mater. **14**, 421 (2014).
[48] Z. Fei *et al.*, Nano Lett. **15**, 4973 (2015).
[49] S. Dai *et al.*, Nat. Nanotechnol **10**, 682 (2015).
[50] S. Dai *et al.*, Science **343**, 1125 (2014).
[51] J. Xia *et al.*, FlatChem **4**, 1 (2017).
[52] C. Ataca, M. Topsakal, E. Aktűrk, and S. Ciraci, The Journal of Physical Chemistry C **115**, 16354 (2011).
[53] L. Novotny, Am. J. Phys. **78**, 1199 (2010).
[54] M. Hertzog *et al.*, Chem. Soc. Rev. **48**, 937 (2019).
[55] P. Törmä and W. L. Barnes, Rep. Prog. Phys. **78**, 013901 (2014).
[56] O. Bitton *et al.*, Nanophotonics **8**, 559 (2019).
[57] Although in this paper we only address wc, sc and usc regimes, the deep-strong coupling (dsc), experimentally achieved in 2017 [94], is stronger then those threes.
[58] A. F. Kockum *et al.*, Nat. Rev. Phys. **1**, 19 (2019).
[59] S. Haastrup *et al.*, 2D Mater. **5**, 042002 (2018).
[60] M. N. Gjerding *et al.*, J. Phys. Chem. **124**, 11609 (2020).
[61] K. Andersen *et al.*, Nano Lett. **15**, 4616 (2015).
[62] A. L. Fetter, *Quantum Theory of Many-Particle Systems* (Dover Publications Inc., 2003).
[63] E. H. Hwang and S. D. Sarma, Phys. Rev. B **75**, 075418 (2007).
[64] B. Wunsch *et al.*, New J. Phys. **8**, 318 (2006).
[65] A. Principi *et al.*, Phys. Rev. B **80**, 075418 (2009).
[66] A. Tomadin *et al.*, Phys. Rev. Lett. **115**, 087401 (2015).
[67] A. Laturia *et al.*, NPJ 2D **2**, 6 (2018).
[68] L. S. R. Cavalcante *et al.*, Phys. Rev. B **97**, 125427 (2018).
[69] S. Ribeiro *et al.*, Photonics **7**, 19 (2020).
[70] W. Zhao *et al.*, Nanoscale **5**, 9677 (2013).
[71] A. Molina-Sánchez and L. Wirtz, Phys. Rev. B **84**, 155413 (2011).
[72] B. Peng *et al.*, RSC Advances **6**, 5767 (2016).
[73] A. Berkdemir *et al.*, Sci. Reps **3**, 1 (2013).
[74] A. Sengupta *et al.*, AIP Advances **5**, 027101 (2015).
[75] L. S. R. Cavalcante *et al.*, J. Phys. Chem. C **123**, 16373 (2019).
[76] I. R. Lavor *et al.*, 2D Mater. **8**, 015014 (2020).
[77] S. N. Shirodkar *et al.*, Phys. Rev. B **97**, 195435 (2018).
[78] H. C. Nerl *et al.*, NPJ 2D Mater. Appl. **1**, 2 (2017).
[79] The dielectric building blocks and QEH software can be downloaded at https://cmr.fysik.dtu.dk/vdwh/vdwh.html.
[80] D. J. Griffiths, *Introduction to Electrodynamics* (Cambridge University Press, 2017).
[81] M. O'Brien, N. McEvoy, D. Hanlon, T. Hallam, J. N. Coleman, and G. S. Duesberg, Scientific reports **6**, 1 (2016).
[82] T. Sriv, K. Kim, and H. Cheong, Scientific reports **8**, 1 (2018).
[83] L. Liang, J. Zhang, B. G. Sumpter, Q.-H. Tan, P.-H. Tan, and V. Meunier, ACS nano **11**, 11777 (2017).
[84] Y. Jia *et al.*, ACS Photonics **2**, 907 (2015).
[85] C. Huck *et al.*, Opt. Express **24**, 25528 (2016).
[86] T. Low *et al.*, Phys. Rev. Lett. **112**, 116801 (2014).
[87] M. Ceriotti, F. Pietrucci, and M. Bernasconi, Physical Review B **73**, 104304 (2006).
[88] Y. Cai, J. Lan, G. Zhang, and Y.-W. Zhang, Physical Review B **89**, 035438 (2014).
[89] D. Yoo, F. de León-Pérez, M. Pelton, I.-H. Lee, D. A. Mohr, M. B. Raschke, J. D. Caldwell, L. Martín-Moreno, and S.-H. Oh, Nature Photonics **15**, 125 (2020).
[90] J. L. Verble and T. J. Wieting, Physical Review Letters **25**, 362 (1970).
[91] J. Ribeiro-Soares, R. M. Almeida, E. B. Barros, P. T. Araujo, M. S. Dresselhaus, L. G. Cançado, and A. Jorio, Physical Review B **90**, 115438 (2014).
[92] G. Froehlicher, E. Lorchat, F. Fernique, C. Joshi, A. Molina-Sánchez, L. Wirtz, and S. Berciaud, Nano Letters **15**, 6481 (2015).
[93] G. Plechinger, S. Heydrich, J. Eroms, D. Weiss, C. Schüller, and T. Korn, Applied Physics Letters **101**, 101906 (2012).
[94] F. Yoshihara *et al.*, Nature Physics **13**, 44 (2016).